remote sensing

MDPI

Article

Seasonal Comparison of the Wildfire Emissions in Southern African Region during the Strong ENSO Events of 2010/11 and 2015/16 Using Trend Analysis and Anomaly Detection

Lerato Shikwambana [1,2,*] and Mahlatse Kganyago [3]

1 Earth Observation Directorate, South African National Space Agency, Pretoria 0001, South Africa
2 School of Geography, Archaeology and Environmental Studies, University of the Witwatersrand, Johannesburg 2050, South Africa
3 Department of Geography, Environmental Management and Energy Studies, University of Johannesburg, Johannesburg 2092, South Africa
* Correspondence: lshikwambana@sansa.org.za

Abstract: This study investigates the wildfire biomass-burning emission levels during strong El Niño–southern oscillation (ENSO) events of 2010–2011 (characterized by a strong La Niña event) and 2015–2016 (characterized by a strong El Niño event) over the southern African region. Specifically, the biomass-burning parameters of black carbon (BC), carbon monoxide (CO) and sulfur dioxide (SO_2) were investigated. Of interest in the current study was the strong El Niño (2015–2016) and La Niña (2010–2011) events during the main fire seasons in southern Africa, i.e., June–July–August (JJA) and September–October–November (SON). Furthermore, the study looks at how meteorological parameters (temperature and precipitation) are influenced by the two strong ENSO events. The sequential Mann–Kendall (SQMK) test is used to study the long-term trends of the emission and meteorological parameters. Anomaly detection on the long-term emission trends and meteorological parameters are performed using the seasonal and trend decomposition loess (STL) and generalized extreme studentized deviate (GESD). Overall, the results show higher emission levels of SO_2, CO, and BC during the JJA season compared to the SON season. The SQMK results show an increasing trend of SO_2, CO, and BC over time, indicating an increase in the amount of biomass burning. The GESD showed significant anomalies for BC, SO_2, and CO emanating from the two strong El Niño and La Niña events. On the other hand, no significant anomalies were detected for temperature and precipitation. The results in this study highlight the significant effect of strong ENSO events on wildfire emissions, thus retrospectively showing the potential effect of future events, especially in the context of climate change.

Keywords: ENSO; wildfires; southern Africa; remote sensing; sea surface temperature

check for updates

Citation: Shikwambana, L.; Kganyago, M. Seasonal Comparison of the Wildfire Emissions in Southern African Region during the Strong ENSO Events of 2010/11 and 2015/16 Using Trend Analysis and Anomaly Detection. *Remote Sens.* **2023**, *15*, 1073. https://doi.org/10.3390/rs15041073

Academic Editors: Yu Wu, Fangwen Bao and Jing Wei

Received: 27 January 2023
Revised: 7 February 2023
Accepted: 14 February 2023
Published: 15 February 2023

1. Introduction

The El Niño–southern oscillation (ENSO) is a large-scale climatic occurrence that emanates in the tropical Pacific, but affects various parts of the world's climate patterns [1–3]. Components of ENSO that are strongly related are sea surface temperature (SST), atmospheric pressure, and the Walker circulation [4]. ENSO events can be classified using the Oceanic Niño Index (ONI), which uses three-month running means of SST anomalies in the Niño 3.4 region (5°N to 5°S, 120°W to 170°W) [5]. Monitoring of ENSO conditions primarily focuses on SST anomalies in four geographic regions of the equatorial Pacific [6]. On the positive side, ENSO occurrence, dynamics, and influence are well understood and can be predicted [7]. However, the response of ENSO to global warming is still of great interest for the future climate [8].

When ENSO is inactive, i.e., during a neutral year, the equatorial Pacific trade winds blow from east to west. An east–west difference in SST and sea level pressure is created, thereby maintaining the trade winds. During an El Niño year, the east–west SST and the pressure difference weakens and the trade winds and their effects on the ocean weaken, resulting in further warming of the eastern Pacific [9]. The El Niño event generally results in higher temperatures and reduced precipitation across the tropics [10]. The opposite happens during the La Niña year: the east–west difference in temperature strengthens, the pressure difference strengthens, and the trade winds and their effects on the ocean strengthen, so the east Pacific cools further. ENSO robustly modulates global drought, temperature, tropical cyclones, precipitation, extratropical cyclones, tornadoes, and other extreme events [11]. ENSO also plays an important role in global warming projections.

The Summary for Policymakers (SPM) presented by the Working Group I (WGI) contribution to the Intergovernmental Panel on Climate Change (IPCC) Sixth Assessment Report (AR6) on the physical science basis of climate change shows that "the last four decades have been successively warmer than any decade that preceded it since 1850" [12]. The report further showed that the increases in well-mixed greenhouse gas (GHG) concentrations since around 1750 are unequivocally caused by human activities [12]. The report also showed that human influence (such as biomass burning (BB)) has warmed the climate at a rate that is unprecedented in at least the last 2000 years [12]. Wildfire BB emission directly influences climate change [13,14].

Wildfires release large quantities of gaseous pollutants and aerosol particles to the atmosphere that have a substantial impact on air quality and human health [15,16]. When burned, biomass material releases widespread varieties of gases such as carbon monoxide (CO), black carbon (BC), carbon dioxide (CO_2), methane (CH_4), smoke, volatile and semi-volatile organic compounds, aldehyde, organic acid and inorganic elements, and particulate matter (PM) [17]. These pollutants can be transported over long distances and affect regions farther away from the source area [18]. Bai et al. [19] explored the relationship between disturbances caused by forest insect–fire interactions and ENSO using fire-burned area, insect-damaged area, average temperature, diurnal temperature range, precipitation, and self-calibrated Palmer Drought Severity Index in China. Their study found a significant correlation between forest insect and fire damage and ENSO during spring. In another study, Burton et al. [20] evaluated the effects of the 2015/16 El Niño on precipitation, temperature, and burned area globally with a specific focus on South America, Africa, and Asia using a dynamic land surface model. Their model projected a variable response in precipitation, with some areas including southern Africa becoming drier, and causing a wider burned area during El Niño conditions. African regions exhibited variable (i.e., lower and higher) burned areas. Shikwambana et al. [21] examined the spatio-temporal properties of wildfires during the recent strong ENSO events using various emission and burned area parameters, but did not show the seasonal variation and trends of these emission parameters, which may be interesting for wildfire management and conservation authorities.

Satellite sensors are the favored way to measure pollutants and detect their transport as they provide frequent and comprehensive observations [22]. They further enable the observation-based tracking of pollutants with relatively high spatial resolution. However, some sensors are based on coarse spatial resolution images ($\geq$500 m), which may have significant omission and commission errors, particularly where fires are small [23]. Some of the satellite sensors that have been used to measure pollutants from wildfires include the moderate resolution imaging spectroradiometer (MODIS) [24], Cloud–Aerosol Lidar with Orthogonal Polarization (CALIOP) [25], atmospheric infrared sounder (AIRS) [26], and, more recently, the tropospheric monitoring instrument (TROPOMI) [27]. Furthermore, wildfire risk has climate drivers of high wind speed, lightning, relative humidity, high temperature, and low precipitation [28], which can be measured by satellite sensors. Reanalysis products from the Modern-Era Retrospective Analysis for Research and Applications, version 2 (MERRA-2) have also been used [29].

Against this background knowledge, this study aims at comparing the wildfire BB emissions during the two strong ENSO events of 2010/11 (i.e., La Niña) and 2015/16 (i.e., El Niño) over the southern African region. Specifically, the spatial distribution of

BC, CO, and SO_2 are examined during the main wildfire seasons, i.e., June–July–August (JJA) and September–October–November (SON), as previously identified by Kganyago and Shikwambana [30]. In addition, meteorological parameters, i.e., temperature and precipitation's spatial distributions in relation to emission hotspots and trends, are also investigated. To our knowledge only a limited number of studies of this nature have been carried out in southern Africa. The study contributes to a better understanding of regional BB emission patterns in response to strong ENSO events.

2. Study Area

The climates in southern Africa (0°–34°S) are seasonal, ranging from arid to semi-arid, and from temperate to tropical [31]. The region is already highly exposed to the effects of ENSO. The ENSO cycles respectively cause severe droughts and floods in the region. They are a major driver of climate variability, which is partly responsible for food insecurity [32]. Moreover, the southern African climate is also impacted to a lesser extent by the Southern Annular Mode (SAM) and SST dipole events in the Indian and South Atlantic Oceans [31]. The other two unique regional ocean features imprint on the climate of southern Africa are the Angola–Benguela Frontal Zone (ABFZ) and the Seychelles–Chagos thermocline ridge (SCTR) [32–35].

3. Data and Methods

3.1. Data

The data used in this study are summarized in Table 1. This table illustrates the products with their spatial and temporal resolution. The CO, BC, SO_2, temperature, and precipitation data are also used in the statistical trend analysis.

Table 1. Summary of the parameters used in this study.

Input Data Source (Temporal Acquisition, Spatial Resolution)	Products Used	Time of Analysis	Deliverables
The Modern-Era Retrospective Analysis for Research and Applications, Version 2 (Merra-2) (monthly; 0.5° × 0.625°)	(a) CO emissions ($kg{\cdot}m^{-2}{\cdot}s^{-1}$) (b) BC and SO_2 biomass-burning emissions ($kg{\cdot}m^{-2}{\cdot}s^{-1}$)	2010/2011 and 2015/2016	(a) Spatial distribution maps of CO emissions (b) BC and SO_2 distribution maps of biomass-burning emissions
Cloud–Aerosol Lidar and Infrared Pathfinder Satellite Observations (CALIPSO) (monthly,2° × 5°)	(a) AOD mean elevated smoke	2010/2011 and 2015/2016	(a) Spatial distribution maps of AOD mean smoke
Atmospheric Infrared Sounder (AIRS) (monthly, 13.5 km at nadir, 1 km vertical)	Air temperature (°C)	2010/2011 and 2015/2016	Spatial distribution maps of air temperature
Tropical Rainfall Measuring Mission (TRMM) (monthly, 0.25° × 0.25°)	Precipitation rate (mm/month)	2010/2011 and 2015/2016	Spatial distribution maps of the precipitation rate

3.1.1. MERRA-2

The Modern-Era Retrospective Analysis for Research and Applications, Version 2 (MERRA-2) is the first long-term global reanalysis to assimilate space-based observations of aerosols and represent their interactions with other physical processes in the climate system [36]. MERRA-2 is produced with the Global Modeling and Assimilation Office (GMAO)/GEOS-5 (Goddard Earth Observing System Data Assimilation System Version 5) Data Assimilation System Version 5.12.4 and its natural resolution is 0.5° × 0.625° × 72 hybrid sigma/pressure levels. Hourly data intervals are used for two-dimensional products, while three-hourly intervals are used for three-dimensional products [37]. More details on MERRA-2 can be found in Gelaro et al. [37], Buchard et al. [38], and Randles et al. [39]. The datasets used in this study are BC and SO_2 BB emissions, and CO emission. Many studies have proven the reliability of MERRA-2 data by determining the correlation between BC concentrations from MERRA-2 reanalysis data and ground measurements [40]

(Yan et al., 2022). Therefore, the reliability of MERRA-2 data for BC is authentic and trustworthy. However, MERRA-2 aerosol analysis corrects aerosol loadings, but does not assimilate any SO_2 and CO observations. Thus, SO_2 and CO concentrations are completely unconstrained [39].

3.1.2. CALIPSO/CALIOP

Cloud–Aerosol Lidar with Orthogonal Polarization (CALIOP) is the primary instrument on the Cloud–Aerosol Lidar and Infrared Pathfinder Satellite Observations (CALIPSO) satellite [41]. CALIOP is a two-wavelength (532 nm and 1064 nm) polarization-sensitive lidar that provides high-resolution vertical profiles of aerosols and clouds. CALIOP uses three receiver channels: one measures the 1064 nm backscatter intensity, and two channels measure the orthogonally polarized components of the 532 nm backscattered signal. The receiver telescope is 1 m in diameter. The full-angle field of view of the telescope is 130 μrad, resulting in a footprint at the Earth's surface of about 90 m. The CALIOP level 2 aerosol products provide vertically resolved aerosol extinction as well as aerosol type [41]. There are three types of level 2 data products: layer products, profile products, and the vertical feature mask (VFM). Layer products provide layer-integrated or layer-averaged properties of detected aerosol and cloud layers, profile products provide retrieved extinction and backscatter profiles within these layers, and the VFM provides information on cloud and aerosol locations and types [42]. More details on the algorithm developed to identify aerosol and cloud layers and to retrieve a variety of optical and microphysical properties is discussed by Winker et al. [41] and Vaughan et al. [43]. In this study, we use the AOD mean elevated smoke product.

3.1.3. AIRS

The atmospheric infrared sounder (AIRS) is one of six instruments aboard NASA (the National Aeronautics and Space Administration)'s Aqua satellite, which was launched on 4 May 2002 [44]. AIRS was launched into orbit with the intention of enhancing our understanding of Earth's weather and climate. AIRS has 2378 infrared channels in the spectral range of 3.7 to 15.4 microns, with a spatial resolution of 13.5 km and four Vis/NIR channels from 0.4 to 0.8 microns with a spatial resolution of 2.3 km [45]. More details of the instrument are discussed by Hartmut et al. [46], Chahine et al. [47], and Menzel et al. [48]. In this study, we use the air temperature product.

3.1.4. TRMM

The Tropical Rainfall Measuring Mission (TRMM) was designed to improve the understanding of the distribution and variability of precipitation within the tropics as part of the water cycle in the climate system. TRMM provides precipitation information using several space-borne instruments to increase the understanding of the interactions between the water vapor and clouds that are central to regulating Earth's climate. The five TRMM instruments onboard are the lightning imaging sensor (LIS), TRMM microwave imager (TMI), visible and infrared scanner (VIRS), the precipitation radar (PR), and the Clouds and the Earth's Radiant Energy System (CERES). Kummerow et al. [49] and Liu et al. [50] provide comprehensive details on the specifications of the TMI, PR, VIRS, and LIS instruments.

3.2. Statistical Analysis

3.2.1. SQMK Test

The sequential Mann–Kendall (SQMK) test on time series x detects approximate potential trend change points [51]. This test sets up two series: a progressive $u(t)$ and a retrograde (backward) series $u'(t)$. If they cross each other and diverge beyond the specific threshold value, then there is a statistically significant trend. The point where they cross each other indicates the approximate year (i.e., change point) at which the trend begins [52]. The threshold values in this study are ± 1.96 ($\alpha = 0.05$). The SQMK test is computed using the ranked values y_i of the original values in analysis $(x_1, x_2, x_3, \ldots, x_n)$. The magnitude of

y_i $(i = 1, 2, 3 \ldots, n)$ are compared with y_j $(j = 1, 2, 3, \ldots, i-1)$. For each comparison, the cases where $y_{i>}y_j$ are counted and denoted by n_i. A statistic t_i can therefore be defined as:

$$t_i = \sum_{j=1}^{i} n_j \tag{1}$$

The distribution of test statistic t_i has a mean as

$$E(t_i) = \frac{i(i-1)}{4} \tag{2}$$

and variance as

$$var(t_i) = \frac{i(i-1)(2i+5)}{72} \tag{3}$$

The sequential progressive value can be calculated as

$$u(t_i) = \frac{t_i - E(t_i)}{\sqrt{var(t_i)}} \tag{4}$$

Similarly, the values of $u'(t_i)$ are computed backwards, starting from the end of the series. In this study, the SQMK test was used to test the null hypothesis (H_0) that there is no significant change point in the times of the BB emissions and meteorological parameters at the 95% confidence level.

3.2.2. Anomaly Detection

Anomaly detection is critical for discovering significant or extreme biomass emission events from the time series data. Emissions data were obtained using seasonal and trend decomposition loess (STL) [53] and generalized extreme studentized deviate (GESD) [54]. The STL is a robust non-linear technique for decomposing a time series into seasonal, trend, and remainder components. The seasonal component consists of the variation in the time series data for a given seasonal frequency, e.g., yearly, while the trend component consists of the variation in the time series data in the long-term low-frequency non-stationary level, and the remainder is the remaining portion of the time series that is not trend or season. GESD identifies multiple anomalies (or outliers) in time series observations by ranking them according to the order of deviation from the mean [55]. The GESD test assumes the normal distribution of a univariate dataset, and using Equation 5, it tests the null hypothesis (H_0) that no outliers exist in the data, while the alternative hypothesis (H_1) is that one or more outliers exist in the data.

$$R_i = max_{i \in \{1,\ldots,n\}} \frac{|x_i - \overline{x}|}{s} \tag{5}$$

where s and $\overline{x}$ are the sample standard deviation and mean, respectively. Given an upper bound, r, for the number of suspected anomalies, the GESD test essentially performs r separate tests; it then removes the observation that maximizes $|x_i - \overline{x}|$ and recomputes the above statistic with $n-1$ observations. It repeats this process until r observations have been removed, resulting in the r test statistics $R_1, R_2, \ldots, R_r$. Consistent with the test statistics, the test computes the critical values as follows:

$$\lambda_i = \frac{(n-i) \times t_p,\ n-i-1}{\sqrt{\left(n-i-1+t_{p,n-i-1}^2\right) \times (n-i+1)}},\ i = 1, 2, \ldots, r \tag{6}$$

where $t_{p,v}^2$ is the $100p$ percentage point from the t distribution with v degrees of freedom and $p = 1 - \frac{\alpha}{2(n-i-1)}$. The number of outliers is determined by finding the largest i, such that $R_i > \lambda_i$. The anomaly detection analysis was performed in R-Statistics version 4.2.2 using the packages “Anomaly Detection” and “Anomalize”.

4. Results

4.1. Trend Analysis

Time series plots of the progressive $u(t)$ and retrograde $u'(t)$ series values are shown in Figures 1 and 2, and the associated interannual variability can be observed in Figures 3 and 4. The results of the SQMK test for emission datasets in southern Africa detect the statistically significant change points in the annual trends for BC biomass-burning emissions (see Figure 1a), CO emissions (see Figure 1b), and SO_2 biomass-burning emissions (see Figure 1c). The progressive series shows that BC and SO_2 biomass-burning emissions have two intersection points in 2007 and 2011, respectively (see Figure 1a). However, these intersections do not occur within the defined confidence interval of ± 1.96 at $\alpha = 0.05$, indicating that the change point is not significant at the 95% confidence level. BC and SO_2 biomass-burning emissions increase from 2008, but become statistically significant after 2016. CO emissions (see Figure 1c) show an intersection within the confidence interval in 2008, indicating a change point. An increasing trend from 2007 is also observed and becomes statistically significant in 2015. The retrograde series shows a decrease in BC and SO_2 biomass-burning emission during the La Niña period and an increase during the El Niño period. CO emissions also show the same trend. Therefore, for these emission parameters, the SQMK test rejected the null hypothesis at the 95% confidence level.

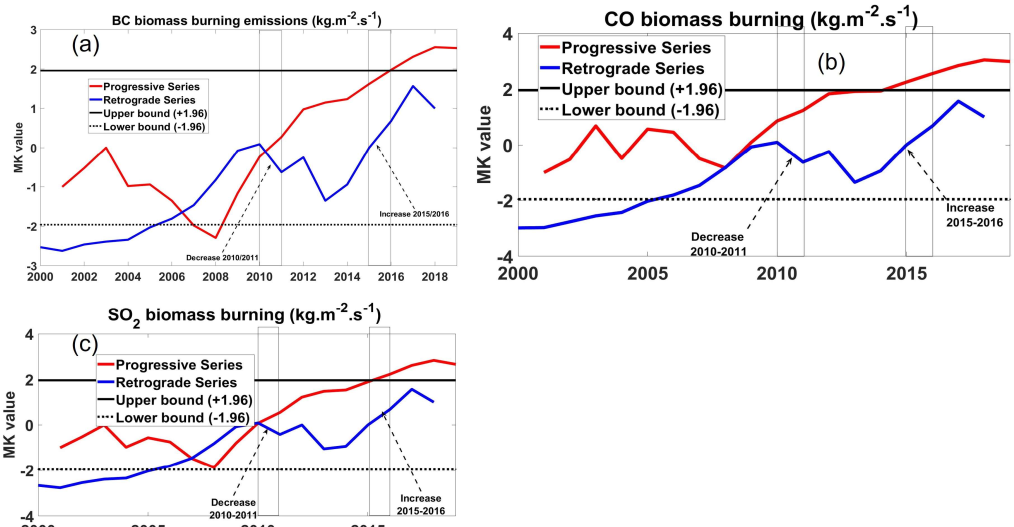

Figure 1. Trends in southern Africa for (**a**) BC biomass-burning emissions, (**b**) CO emissions, and (**c**) SO_2 biomass-burning emissions derived from sequential Mann–Kendal test statistics.

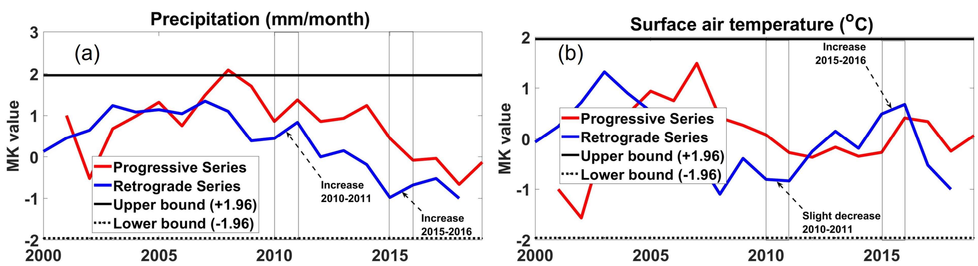

Figure 2. Trends in southern Africa for (**a**) precipitation and (**b**) surface air temperature derived from sequential Mann–Kendal test statistics.

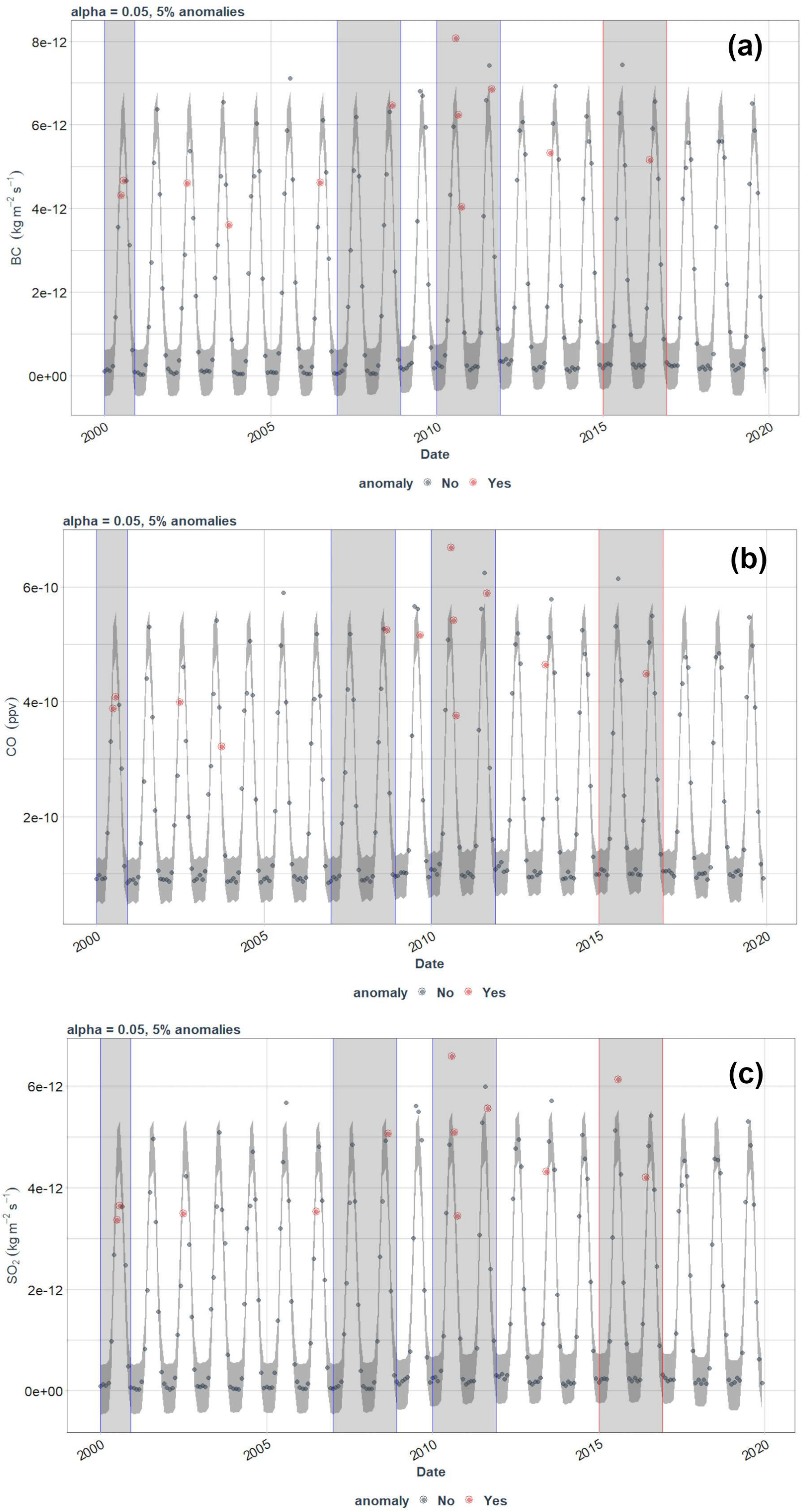

Figure 3. Interannual variability and emissions anomalies detected by generalized extreme studentized deviate (GESD) from 2000 to 2020. (**a**) Black carbon (BC), (**b**) carbon monoxide (CO), and (**c**) sulfur dioxide (SO_2).

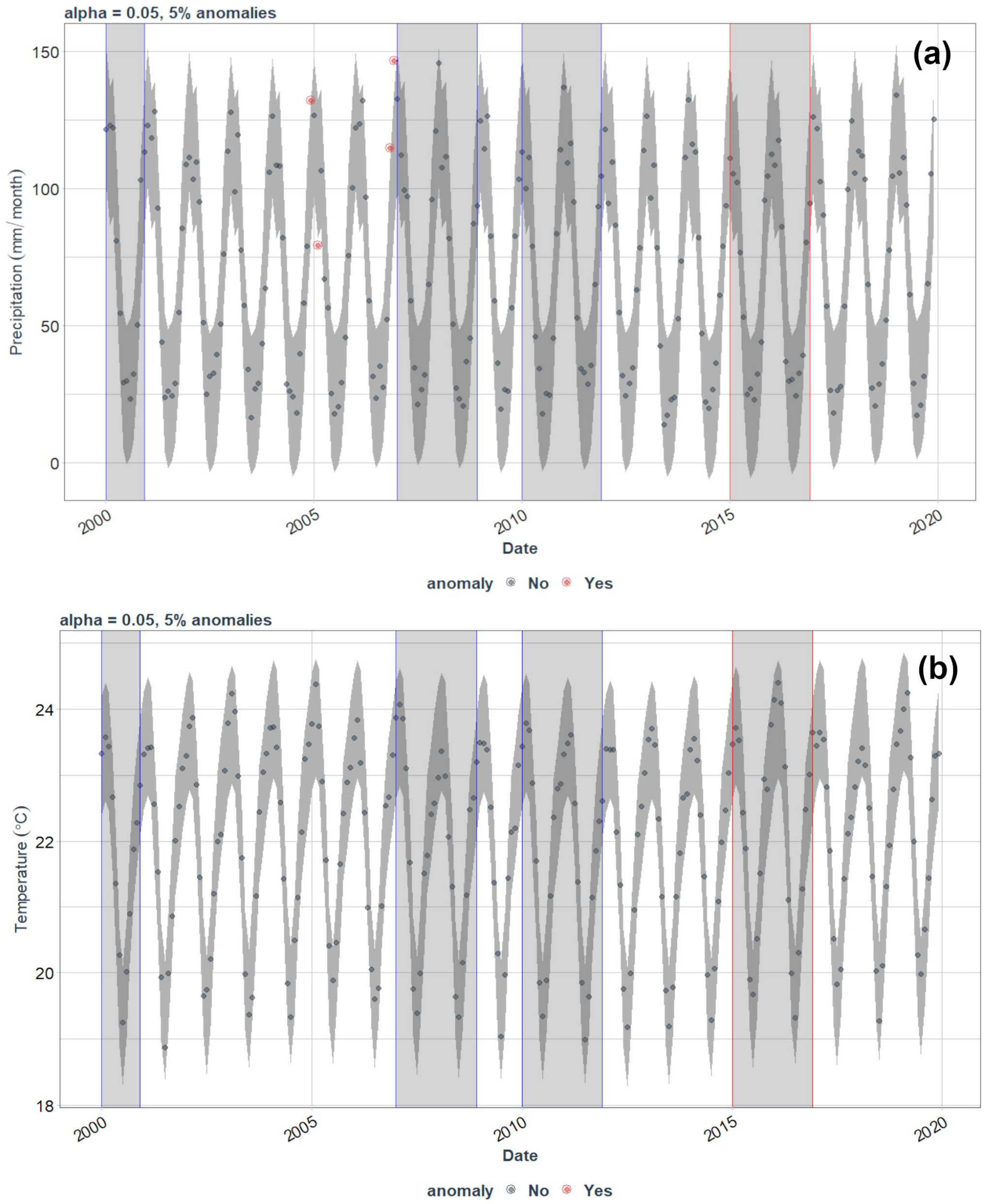

Figure 4. Interannual variability and anomalies of meteorological parameters detected by generalized extreme studentized deviate (GESD) from 2000 to 2020. (**a**) Precipitation (PCPN) and (**b**) temperature.

The progressive $u(t)$ and retrograde $u'(t)$ curves of precipitation (see Figure 2a) and temperature (see Figure 2b) do not indicate any significant trends. The overall trend for precipitation exhibits a slight decrease over the period, whereas the temperature does not show any significant trend. Therefore, the SQMK test for precipitation and temperature failed to reject the null hypothesis at the 95% confidence level. The summary of the SQMK results is shown in Table 2. The precipitation trends show a slight increase in the La Niña and El Niño periods. The temperature shows a slight decrease in the La Niña period and an increase in the El Niño period.

Table 2. Intersection points by sequential Mann–Kendall test for southern Africa (values significant at $p \leq 0.05$).

Parameters	Intersection Points			Remarks
	1st	2nd	3rd	
BC	2007	2011	——	Significant
SO_2	2007	2011	——	Significant
CO	2007	——	——	Significant
Precipitation	2001	2004	2007	——
Temperature	2005	2012	2016	——

4.2. Anomaly Detection

The results for anomaly detection using generalized extreme studentized deviate (GESD) are presented in Figures 3 and 4. As shown in Figure 3, the greatest emission anomalies are observed during a period consistent with strong El Niño and La Niña events. For all of the emission parameters considered here, the La Niña event of 2010–2011 shows several and highest anomalies relative to those detected during the strong El Niño event in 2015–2016. For BC, the significant anomalies were detected in 2000 (i.e., July and August), 2002 (i.e., July), 2003 (October), 2006 (i.e., July), 2008 (September), 2010 (August, September, and October), 2011 (i.e., September), 2013 (June), and 2016 (June). For CO, the significant anomalies were detected in times consistent with BC, except that additional significant anomalies were also detected in 2009 (September) and no anomalies were detected in 2006. Lastly, the SO_2 anomalies were also consistent with BC anomalies, except that no significant anomalies were detected in 2003 and anomalies were also detected in 2015 (August). On the other hand, no significant anomalies were detected in the meteorological parameters during the strong ENSO events (see Figure 4).

4.3. Spatial Distribution of Emission and Meteorological Parameters during JJA and SON

Since we observed the significant change points (based on SQMK test) and highest anomalies during the years 2010/11 and 2015/16, we further analyzed the seasonal variations of the emissions, particularly focusing on the June–July–August (JJA) and September–October–November (SON) periods, which are the main fire seasons in southern Africa as observed by Kganyago and Shikwambana (2019). Figure 5 shows the spatial distribution of BC biomass-burning emissions during the JJA and SON seasons during the strong La Niña and El Niño events. A high BB emission of BC is observed during the JJA season for both ENSO events (see Figure 5a,b). A BC plume in the JJA season is mainly attributed to the burning of vegetation [56]. A slightly larger BC biomass-burning emissions distribution (1.5×10^{-10} kg.m^{-2}.s^{-1}) is observed in the La Niña event compared to the BC distribution in the El Niño event. In the La Niña event, BC biomass-burning emissions are observed in Botswana and not observed during the El Niño event. The La Niña event is wetter, which allows for vegetation to grow, while the opposite is true for El Niño, therefore less vegetation is present, resulting in less BC biomass burning. On the other hand, during the SON season in both ENSO events, low BC biomass-burning emissions of ~0.5×10^{-10} kg·m^{-2}·s^{-1} is observed (see Figure 5c,d). The results for other emission parameters, i.e., SO_2 biomass-burning emissions (see Figure 6) and CO emissions (see Figure 7) also show similar patterns, i.e., higher emissions in JJA than SON seasons.

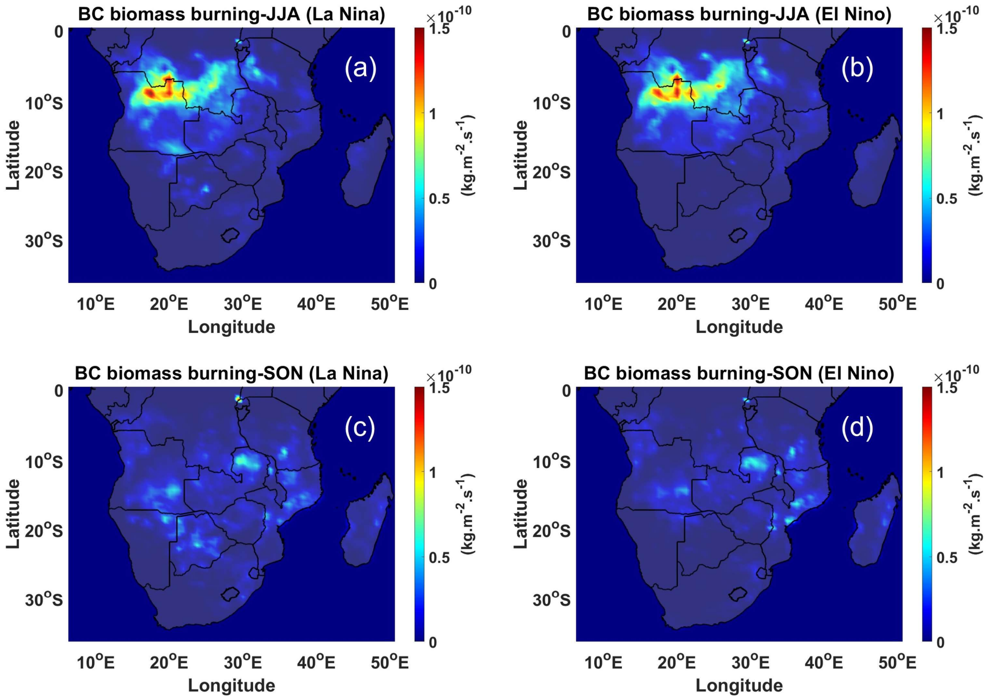

Figure 5. Spatial distribution of BC biomass-burning emissions for the June–July–August (JJA, (**a**,**b**) and September–October–November (SON, (**c**,**d**)) seasons during the La Niña (**a**,**c**) and El Niño (**b**,**d**) events.

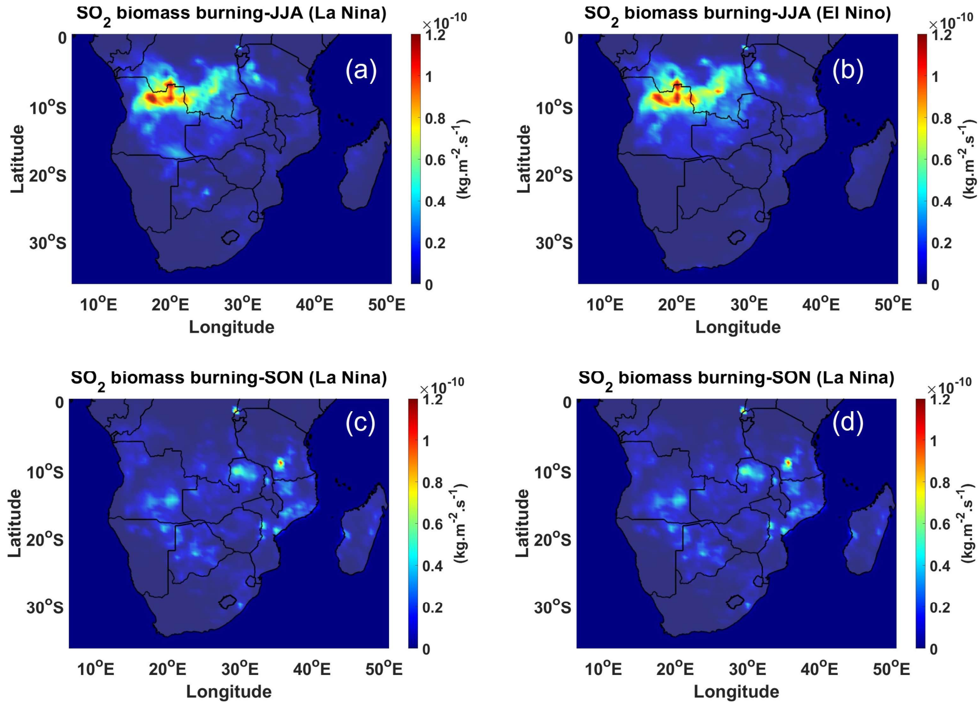

Figure 6. Spatial distribution of SO_2 biomass-burning emissions for the JJA (**a**,**b**) and SON (**c**,**d**) seasons during the La Niña (**a**,**c**) and El Niño (**b**,**d**) events.

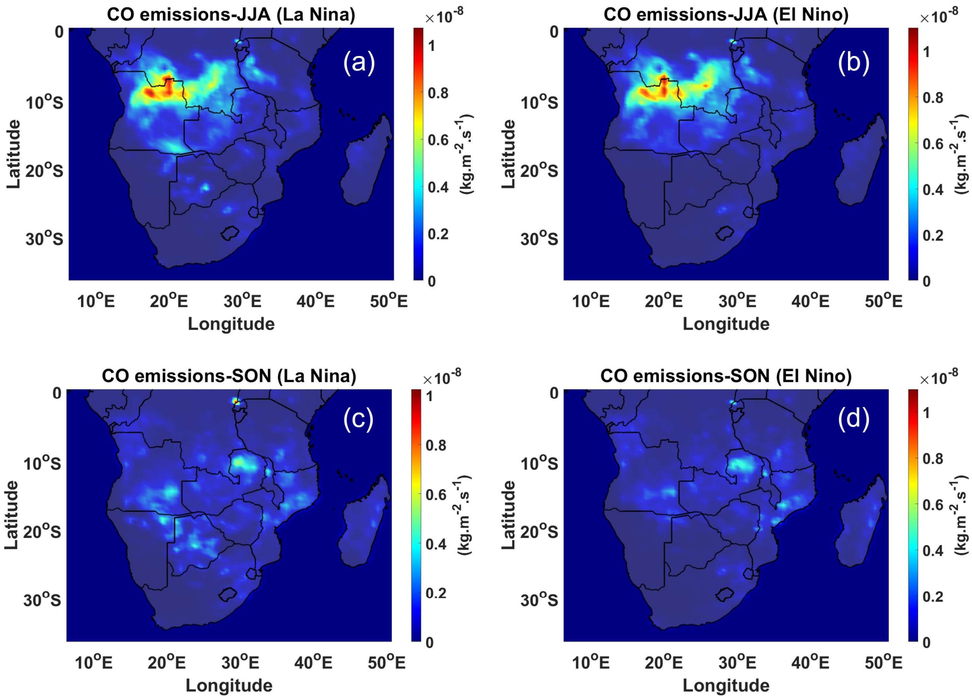

Figure 7. Spatial distribution of CO emissions for the JJA (**a**,**b**) and SON (**c**,**d**) seasons during the La Niña (**a**,**c**) and El Niño (**b**,**d**) events.

The seasonal spatial distribution results in Figures 5–7 are consistent with the higher anomalies observed during La Niña than the El Niño event. The elevated smoke AOD during the strong ENSO events for the seasons of JJA and SON is shown in Figure 8. A high smoke AOD of 0.7 is observed during the JJA season for both the La Niña and El Niño periods (see Figure 8a,b). Surprisingly, the highest smoke AOD of 0.7 is observed during the La Niña period compared to the smoke AOD value of ~0.6 during the El Niño period. This is because burning wet and/or damp wood produces more smoke than burning dry wood; therefore, the La Niña period will produce more smoke AOD. Compared to the JJA season, the SON season (see Figure 8c,d) produces a moderate smoke AOD during the La Niña and El Niño events. La Niña shows smoke AOD values of ~0.45, while El Niño has a smoke AOD value of ~0.35. Again, La Niña shows slightly higher smoke AOD values. The smoke is produced primarily from the burning of vegetation. Smoke, in general, is produced when biomass does not burn completely. Dry biomass burns more, thus producing less smoke compared to wet wood, which does not burn completely and produces more smoke [57]. Smoke perturbs atmospheric radiation through its effects on light extinction and cloud properties [58].

The spatial distributions of temperature and precipitation in the JJA and SON seasons during the La Niña and El Niño periods are shown in Figures 9 and 10. A noticeable temperature difference between La Niña and El Niño events in some parts of southern Africa during the JJA is observed (see Figure 9a,b). The dashed boxes and red arrows show the regions where discernible changes occurred. During the La Niña period (2010–2011), a relatively lower temperature of ~12 °C is observed in the Angola region (dashed box), whereas a higher temperature of ~20 °C in the same region is observed during the El Niño event (2015–2016). Similar results are observed in the Republic of South Africa (see red arrows), which also shows slightly lower temperatures ~9 °C during the La Niña event and a slightly higher temperature of ~11 °C in the same region during the El Niño period. In the Democratic Republic of Congo (DRC), i.e., where high emission plumes were observed, the temperatures are consistently high between the two ENSO events. Generally, the comparison of the temperature shows lower temperatures during the JJA seasons.

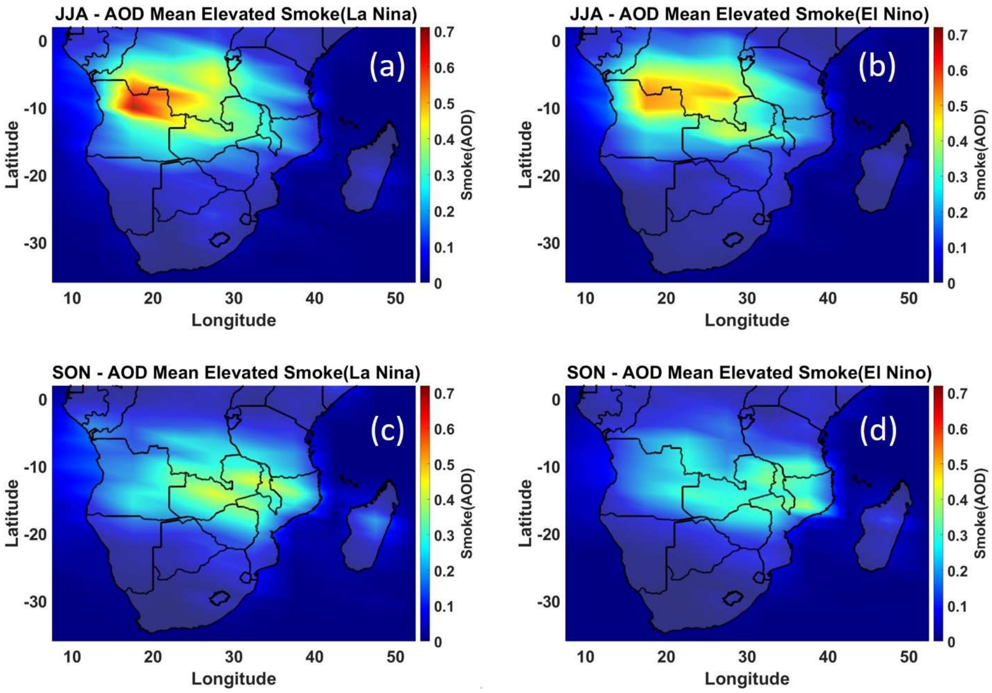

Figure 8. Spatial distribution of AOD mean elevated smoke for the JJA (**a**,**b**) and SON (**c**,**d**) periods during the La Niña (**a**,**c**) and El Niño (**b**,**d**) events.

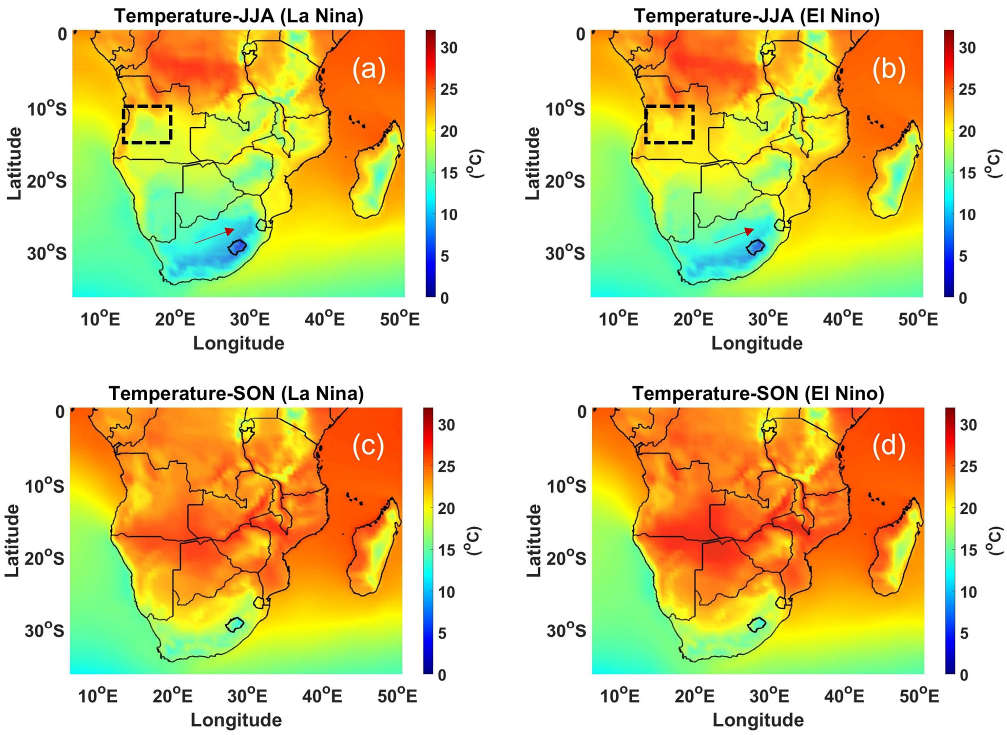

Figure 9. Spatial distribution of temperature for the JJA (**a**,**b**) and SON (**c**,**d**) periods during the La Niña (**a**,**c**) and El Niño (**b**,**d**) events.

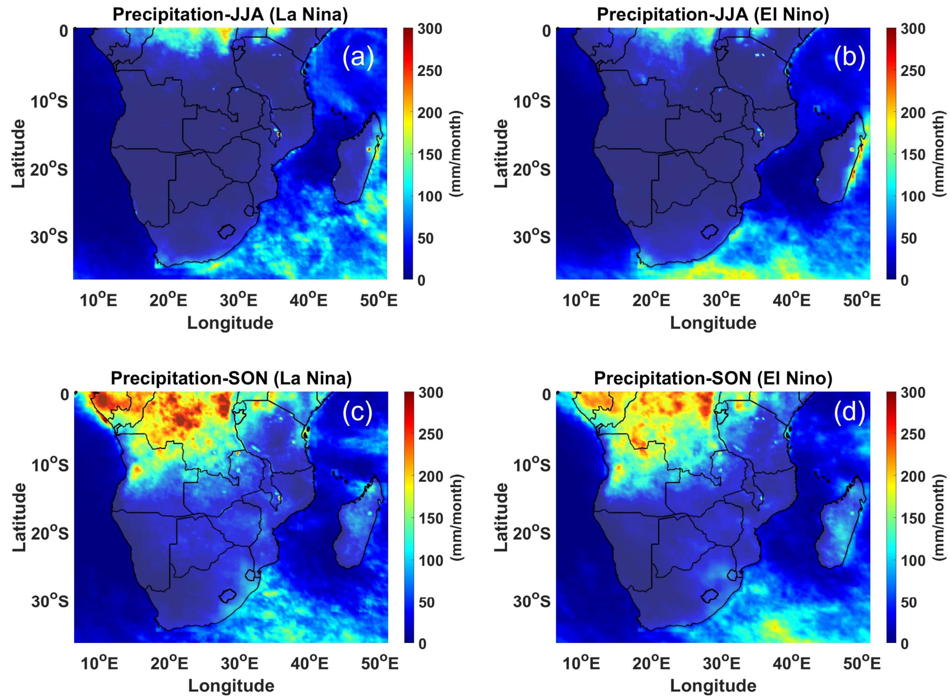

Figure 10. Spatial distribution of precipitation for the JJA (**a**,**b**) and SON (**c**,**d**) seasons during the La Niña (**a**,**c**) and El Niño (**b**,**d**) events.

Figure 10 shows the spatial distribution of precipitation in the JJA and SON seasons during the strong La Niña and El Niño events. Overall, the JJA season shows low to moderate precipitation (between 0 and 150 mm/month) compared to the SON season. SON has moderate to high precipitation (between 150 and 300 mm/month). Moreover, the La Niña period shows more precipitation than the El Niño period.

5. Discussion

ENSO is one of the most vital and longest-studied climate phenomena due to its ability to influence temperatures and precipitation across the globe. Numerous severe and prolonged ENSO events have been recorded throughout time, as well as some notable extreme El Niño events (1982–1983, 1997–1998) and La Niña events (1988–1989, 1973–1974). Recently, the 2015–2016 El Niño is known to be the strongest on record, while the 2010–2011 La Niña is of interest because of its recency. However, studies assessing the influence of the strong ENSO events on BB emissions are rare in Africa. In the current study, trend analysis and anomaly detection were carried out to evaluate whether these ENSO events caused significant anomalies and changes (in magnitude and direction) in BB emissions and meteorological parameters. Moreover, we used several parameters to characterize the spatial distribution of CO, BC, SO_2, temperature, and precipitation during the 2010–2011 and 2015–2016 ENSO events.

According to the results, the BB emission trends were significant at the 95% confidence level, showing a significant decline during the 2010–2011 La Niña event and increasing trend during the 2015–2016 El Niño event. Our previous related study [21], which did not consider seasonal variations in BB emissions between the two ENSO events, showed that most of the 2010–2011 (i.e., La Niña) BB emissions came from the region above −10°S (northern Angola and DRC), while the 2015–2016 (i.e., El Niño) emissions came mainly from the region below −10°S (Zimbabwe, Botswana, and Zambia). Therefore, the trends observed here can be attributed to such patterns, although the region above −10°S equally releases high BB emissions in both ENSO events. A closer look at the main fire seasons, i.e., JJA and SON, in the current study revealed even more interesting results, showing that BB emissions are high in the JJA rather than SON period. In particular, the BB emissions in JJA are mostly distributed in northern Angola, DRC, parts of Zambia, and Tanzania, while SON's relatively lower emissions (~0.5×10^{-10} kg·m^{-2}·s^{-1}) are mainly from Zambia, Zimbabwe, Botswana, and Mozambique in both ENSO events. A study by Winkler et al. [59] showed a precipitation deficit in southern Africa at a region around −10°S during the onset (i.e., August) of the 2010–2011 La Niña event, which explains the higher emissions during JJA. Our results, therefore, imply a delayed response of wildfires to ENSO in the region below −10°S.

It should be noted that southern Africa is characterized by southern hemisphere summers, where most rainfall occurs between October and March. The SON season, therefore, contains two months from the early summer season (October to December), which is influenced by the extratropical atmospheric circulation [60]. Therefore, the observed higher emissions in JJA than SON indicate the influence of early rains, especially during La Niña events as compared to El Niño events, where rains are frequently late, i.e., occurring in the late summer season (January to March). In Figure 2a, it was shown that the 2010–2011 La Niña event experienced a slight increase in precipitation. These rains mostly affect, as shown by the precipitation results (Figure 10c,d), the tropical regions around −10°S, thus suppressing widespread fires during SON. Fuel moisture content is one of the important factors that determine ignition probability and fire behavior in forest ecosystems [61]. Fuel moisture content is the most critical factor affecting fire ignition [62]. Precipitation influences the moisture content of fuels by cooling down the surface and helping to maintain moisture levels within the fuel itself. It therefore slows down or eradicates the combustion process overall.

The relatively lower precipitation levels and high temperatures during JJA in both ENSO events studied here caused water stress and drastically reduced root-zone soil moisture, eventually leading to low productivity and dry vegetation conditions, thus favoring intense and widespread wildfires, which were detected by the GESD anomaly detection (Figure 3a–c). Indeed, wildfires are modulated by a variety of factors such as relative humidity, wind speed, wind direction, fuel load, fuel moisture, and topography, but as the authors in [58] note, temperature and precipitation are the most important factors in fire behavior. Prolonged high temperatures and low precipitation in either ENSO event can increase aridity by drying out the vegetation, making it an effective fuel in the burning process [63,64], as also shown by Figures 9 and 10. Specifically, the El Niño event has been associated with frequent droughts in southern and eastern Africa for the past decade [65], thus further explaining the results of the current study. Brenner [66] found a positive correlation of 71% between the average central Pacific SST anomaly, explaining up to 50% of the variability in burned areas in Florida.

The GESD anomaly detection highlighted anomalous BB emission values recorded during specific months of the two ENSO events. Therefore, the results are significant for fire management agencies, which can then target such hotspot months to extinguish and control fires. This would ensure that the net carbon dioxide is reduced.

6. Conclusions

This study sought to compare biomass-burning (BB) emissions from wildfires (i.e., BC, CO, and SO_2) and associated meteorological conditions (i.e., temperature and precipitation) during the 2010–2011 La Niña and 2015–2016 El Niño events over the southern African region. The study expands on Shikwambana et al. [21] to focus on fire seasons, trends, and anomalies. It must be emphasized that MERRA-2 products have a notable bias, which may be attributed to the systemic bias of the assimilation system. However, the obtained results do give the correct perspective of the distribution and trends of the pollutants discussed.

Generally, the results showed that all of the BB emission parameters had significant trends at the 95% confidence level, considering the period from 2000 and 2018. During the 2010–2011 La Niña and 2015–2016 El Niño strong ENSO events, a significant decline and increase were observed, respectively. Moreover, we observed higher emissions of SO_2, CO, and BC during the JJA season compared to the SON season, mainly distributed below −10°S (northern Angola and DRC) and above −10°S (Zimbabwe, Botswana, and Zambia) in both ENSO events. The emissions were higher during La Niña, due to observed precipitation deficit observed by Winkler [59] in August of 2010 and high temperatures, which then facilitated expansively spread fires and resulted in high levels of emissions during JJA at regions below −10°S. The anomaly detection using GESD showed significant anomalies for BC, SO_2, and CO emanating from the strong El Niño and La Niña events, which were higher during La Niña than El Niño. The higher emissions during SON at a region below −10°S indicate some prolonged effect of ENSO in this region, while relatively low emissions at a region above −10°S can be attributed to slightly higher precipitation during La Niña that suppressed wildfires. The slightly higher temperature and slightly lower PCPN during the El Niño period favors drier conditions for fires and emissions. On the other hand, no significant anomalies (at 95% confidence) were detected for temperature and PCPN. Overall, this study has provided new insights into the response of BB emissions to the strong ENSO events, focusing on significant fire seasons in southern Africa. The findings warrant further studies in the region, which should use high temporal resolution (i.e., daily) data to understand the intra-season variations in BB emissions and modulating parameters during strong ENSO events. Overall, this study is significant for decision- and policymaking related to climate change mitigation and the reduction of GHG emissions from wildfires.

Author Contributions: Conceptualization, L.S. and M.K.; methodology, L.S. and M.K.; formal analysis, L.S. and M.K.; investigation, L.S. and M.K.; data curation, L.S. and M.K.; writing—original draft preparation, L.S. and M.K.; writing—review and editing, L.S. and M.K. All authors have read and agreed to the published version of the manuscript.

Funding: This research received no external funding. The APC was funded by the South African National Space Agency (SANSA).

Data Availability Statement: The data that support the findings of this study are openly available in https://giovanni.gsfc.nasa.gov/giovanni/ and https://urs.earthdata.nasa.gov/.

Acknowledgments: We acknowledge the GES-DISC Interactive Online Visualization and Analysis Infrastructure (Giovanni) for providing the MERRA-2, TRMM, and AIRS data. The authors also thank the NASA Langley Research Centre Atmospheric Science Data Centre for the CALIPSO data.

Conflicts of Interest: The authors declare no conflict of interest.

References

1. Hanley, D.E.; Bourassa, M.A.; O'Brien, J.J.; Smith, S.R.; Spade, E.R. A quantitative evaluation of ENSO indices. *J. Clim.* **2003**, *16*, 1249–1258. [CrossRef]
2. McPhaden, M.J.; Zebiak, S.E.; Glantz, M.H. ENSO as an Integrating Concept in Earth Science. *Science* **2006**, *314*, 1740–1745. [CrossRef]
3. Latif, M.; Keenlyside, N.S. El Niño/Southern Oscillation response to global warming. *Proc. Natl. Acad. Sci. USA* **2009**, *106*, 20578–20583. [CrossRef] [PubMed]
4. Berhane, F.; Zaitchik, B. Modulation of daily precipitation over East Africa by the Madden-Julian Oscillation. *J. Clim.* **2014**, *27*, 6016–6034. [CrossRef]
5. Barnston, A.G.; Chelliah, M.; Goldenberg, S.B. Documentation of a highly ENSO-related SST region in the equatorial Pacific. *Atmos. Ocean* **1997**, *35*, 367–383.
6. Trenberth, Kevin & National Center for Atmospheric Research Staff (Eds). Last Modified 21 January 2020. "The Climate Data Guide: Nino SST Indices (Nino 1+2, 3, 3.4, 4; ONI and TNI)". Available online: https://climatedataguide.ucar.edu/climate-data/nino-sst-indices-nino-12-3-34-4-oni-and-tni (accessed on 25 July 2022).
7. Wang, C.; Picaut, J. Understanding ENSO physics: A review. In *Earth's Climate: The Ocean-Atmosphere Interaction*; Wang, C., Xie, S.P., Carton, J.A., Eds.; American Geophysical Union: Washington, DC, USA, 2013; pp. 21–48.
8. Kohyama, T.; Hartmann, D.L.; Battisti, D.S. Weakening of nonlinear ENSO under global warming. *Geophys. Res. Lett.* **2018**, *45*, 8557–8567. [CrossRef]
9. Trenberth, K.E. The Definition of El Niño. *Bull. Am. Meteorol. Soc.* **1997**, *78*, 2771–2777. [CrossRef]
10. Chen, Y.; Morton, D.C.; Andela, N.; van der Werf, G.R.; Giglio, L.; Randerson, J.T. A pan-tropical cascade of fire driven by El Niño/Southern Oscillation. *Nat. Clim. Chang.* **2007**, *7*, 906–911. [CrossRef]

11. Lin, J.; Qian, T. Switch Between El Nino and La Nina is Caused by Subsurface Ocean Waves Likely Driven by Lunar Tidal Forcing. *Sci. Rep.* **2019**, *9*, 13106. [CrossRef]
12. IPCC. "Summary for Policymakers" in Climate Change 2021: The Physical Science Basis. In *Contribution of Working Group I to the Sixth Assessment Report of the Intergovernmental Panel on Climate Change*; Masson-Delmotte, V., Zhai, P., Pirani, A., Connors, S.L., Péan, C., Chen, Y., Goldfarb, L., Gomis, M.I., Matthews, J.B.R., Berger, S., et al., Eds.; Cambridge University Press: Cambridge, UK, 2021; *in press*.
13. Westerling, A.L.; Hidalgo, H.G.; Cayan, D.R.; Swetnam, T.W. Warming and earlier spring increase western U.S. Forest wildfire activity. *Science* **2006**, *313*, 940–943. [CrossRef] [PubMed]
14. Trouet, V.; Taylor, A.H.; Wahl, E.R.; Skinner, C.N.; Stephens, S.L. Fire-climate interactions in the American West since 1400 CE. *Geophys. Res. Lett.* **2010**, *37*, L04702. [CrossRef]
15. Crutzen, P.J.; Andreae, M.O. Biomass Burning in the Tropics: Impact on Atmospheric Chemistry and Biogeochemical Cycles. *Science* **1990**, *250*, 1669–1678. [CrossRef]
16. Zhao, H. Chapter 18—Biomass burning emission and impacts on air pollution in China. In *Asian Atmospheric Pollution: Sources, Characteristics and Impacts*; Elsevier: Amsterdam, The Netherlands, 2022; pp. 335–347.
17. Sharratt, B.; Auvermann, B. Dust Pollution from Agriculture. In *Encyclopedia of Agriculture and Food Systems*; Elsevier: Amsterdam, The Netherlands, 2014; pp. 487–504.
18. Tang, Y. Influences of biomass burning during the Transport and Chemical Evolution Over the Pacific (TRACE-P) experiment identified by the regional chemical transport model. *J. Geophys. Res. Atmos.* **2003**, *108*, 8824. [CrossRef]
19. Bai, M.; Wang, X.; Yao, Q.; Fang, K. ENSO modulates interaction between forest insect and fire disturbances in China. *Nat. Hazards Res.* **2022**, *2*, 138–146. [CrossRef]
20. Burton, C.; Betts, R.A.; Jones, C.D.; Feldpausch, T.R.; Cardoso, M.; Anderson, L.O. El Niño Driven Changes in Global Fire 2015/16. *Front. Earth Sci.* **2020**, *8*, 199. [CrossRef]
21. Shikwambana, L.; Kganyago, M.; Xulu, S. Analysis of Wildfires and Associated Emissions during the Recent Strong ENSO Phases in Southern Africa Using Multi-Source Remotely-derived Products. *Geocarto Int.* **2022**. [CrossRef]
22. Chuvieco, E.; Mouillot, F.; van der Werf, G.R.; Miguel, J.S.; Tanase, M.; Koutsias, N.; García, M.; Yebra, M.; Padilla, M.; Gitas, I.; et al. Historical background and current developments for mapping burned area from satellite Earth observation. *Remote Sens. Environ.* **2019**, *225*, 45–64. [CrossRef]
23. Laris, P.S. Spatiotemporal problems with detecting and mapping mosaic fire regimes with coarse-resolution satellite data in savanna environments. *Remote Sens. Environ.* **2005**, *99*, 412–424. [CrossRef]
24. Bencherif, H.; Bègue, N.; Kirsch Pinheiro, D.; du Preez, D.J.; Cadet, J.-M.; da Silva Lopes, F.J.; Shikwambana, L.; Landulfo, E.; Vescovini, T.; Labuschagne, C.; et al. Investigating the Long-Range Transport of Aerosol Plumes Following the Amazon Fires (August 2019): A Multi-Instrumental Approach from Ground-Based and Satellite Observations. *Remote Sens.* **2020**, *12*, 3846. [CrossRef]
25. Martinsson, B.G.; Friberg, J.; Sandvik, O.S.; Sporre, M.K. Five-satellite-sensor study of the rapid decline of wildfire smoke in the stratosphere. *Atmos. Chem. Phys.* **2022**, *22*, 3967–3984. [CrossRef]
26. Shikwambana, L.; Kganyago, M. Observations of Emissions and the Influence of Meteorological Conditions during Wildfires: A Case Study in the USA, Brazil, and Australia during the 2018/19 Period. *Atmosphere* **2021**, *12*, 11. [CrossRef]
27. Lemmouchi, F.; Cuesta, J.; Eremenko, M.; Derognat, C.; Siour, G.; Dufour, G.; Sellitto, P.; Turquety, S.; Tran, D.; Liu, X.; et al. Three-Dimensional Distribution of Biomass Burning Aerosols from Australian Wildfires Observed by TROPOMI Satellite Observations. *Remote Sens.* **2022**, *14*, 2582. [CrossRef]
28. Tomašević, I.Č.; Cheung, K.K.W.; Vučetić, V.; Fox-Hughes, P. Comparison of Wildfire Meteorology and Climate at the Adriatic Coast and Southeast Australia. *Atmosphere* **2022**, *13*, 755. [CrossRef]
29. Yasunari, T.J.; Kim, K.M.; da Silva, A.M.; Hayasaki, M.; Akiyama, M.; Murao, N. Extreme air pollution events in Hokkaido, Japan, traced back to early snowmelt and large-scale wildfires over East Eurasia: Case studies. *Sci. Rep.* **2018**, *8*, 6413. [CrossRef] [PubMed]
30. Kganyago, M.; Shikwambana, L. Assessing Spatio-Temporal Variability of Wildfires and their Impact on Sub-Saharan Ecosystems and Air Quality Using Multisource Remotely Sensed Data and Trend Analysis. *Sustainability* **2019**, *11*, 6811. [CrossRef]
31. Marks, S.E. "Southern Africa". Encyclopedia Britannica, Invalid Date. Available online: https://www.britannica.com/place/Southern-Africa (accessed on 25 July 2022).
32. Climate Diplomacy. Available online: https://climate-diplomacy.org/exhibition/southern-africa (accessed on 25 July 2022).
33. Reason, C. Climate of Southern Africa. Oxford Research Encyclopedia of Climate Science. 2017. Available online: https://oxfordre.com/climatescience/view/10.1093/acrefore/9780190228620.001.0001/acrefore-9780190228620-e-513 (accessed on 25 July 2022).
34. Hermes, J.C.; Reason, C.J.C. The sensitivity of the Seychelles–Chagos thermocline ridge to large-scale wind anomalies. *ICES Mar. Sci.* **2009**, *66*, 1455–1466. [CrossRef]
35. Koseki, S.; Giordani, H.; Goubanova, K. Frontogenesis of the Angola–Benguela Frontal Zone. *Ocean Sci.* **2019**, *15*, 83–96. [CrossRef]
36. Nakkazi, M.T.; Sempewo, J.I.; Tumutungire, M.D.; Byakatonda, J. Performance evaluation of CFSR, MERRA-2 and TRMM3B42 data sets in simulating river discharge of data-scarce tropical catchments: A case study of Manafwa, Uganda. *J. Water Clim. Chang.* **2022**, *13*, 522–541. [CrossRef]

37. Gelaro, R.; McCarty, W.; Suárez, M.J.; Todling, R.; Molod, A.; Takacs, L.; Randles, C.A.; Darmenov, A.; Bosilovich, M.G.; Reichle, R.; et al. The Modern-Era Retrospective Analysis for Research and Applications, Version 2 (MERRA-2). *J. Clim.* **2017**, *30*, 5419–5454. [CrossRef]
38. Buchard, V.; Randles, C.A.; da Silva, A.M.; Darmenov, A.; Colarco, P.R.; Govindaraju, R.; Ferrare, R.; Hair, J.; Beyersdorf, A.J.; Ziemba, L.D.; et al. The MERRA-2 Aerosol Reanalysis, 1980 Onward. Part II: Evaluation and Case Studies. *J. Clim.* **2017**, *30*, 6851–6872. [CrossRef]
39. Randles, C.A.; da Silva, A.M.; Buchard, V.; Colarco, P.R.; Darmenov, A.; Govindaraju, R.; Smirnov, A.; Holben, B.; Ferrare, R.; Hair, J.; et al. The MERRA-2 Aerosol Reanalysis, 1980 Onward. Part I: System Description and Data Assimilation Evaluation. *J. Clim.* **2017**, *30*, 6823–6850. [CrossRef] [PubMed]
40. Yan, G.; Hao, Y.; Li, M.; Zheng, X.; Li, S.; Yao, D.; Liu, M.; Hu, P. Pollution characteristics of black carbon based on MERRA-2 reanalysis data in core city of Central Plains Economic Zone, China: Historical trend and potential sources. *Front. Environ. Sci.* **2022**, *10*, 2253. [CrossRef]
41. Winker, D.M.; Vaughan, M.A.; Omar, A.; Hu, Y.; Powell, K.A.; Liu, Z.; Hunt, W.H.; Young, S.A. Overview of the CALIPSO Mission and CALIOP Data Processing Algorithms. *J. Atmos. Ocean Technol.* **2009**, *26*, 2310–2323. [CrossRef]
42. Omar, A.H.; Winker, D.M.; Vaughan, M.A.; Hu, Y.; Trepte, C.R.; Ferrare, R.A.; Lee, K.P.; Hostetler, C.A.; Kittaka, C.; Rogers, R.R.; et al. The CALIPSO Automated Aerosol Classification and Lidar Ratio Selection Algorithm. *J. Atmos. Ocean Technol.* **2009**, *26*, 1994–2014. [CrossRef]
43. Vaughan, M.A.; Powell, K.A.; Kuehn, R.E.; Young, S.A.; Winker, D.M.; Hostetler, C.A.; Hunt, W.H.; Liu, Z.Y.; McGill, M.J.; Getzewich, B.J. Fully Automated Detection of Cloud and Aerosol Layers in the CALIPSO Lidar Measurements. *J. Atmos. Ocean. Technol.* **2009**, *26*, 2034–2050. [CrossRef]
44. Aumann, H.H.; Chahine, M.T.; Gautier, C.; Goldberg, M.D.; Kalnay, E.; McMillin, L.M.; Revercomb, H.; Rosenkranz, P.W.; Smith, W.L.; Staelin, D.H.; et al. AIRS/AMSU/HSB on the aqua mission: Design, science objectives, data products, and processing systems IEEE Trans. *Geosci. Remote Sens.* **2003**, *41*, 253–264. [CrossRef]
45. Pagano, T.S.; Aumann, H.H.; Gaiser, S.L.; Gregorich, D.T. Early calibration results from the atmospheric infrared sounder (AIRS) on Aqua. In Proceedings of the SPIE 4891, Optical Remote Sensing of the Atmosphere and Clouds III, Hangzhou, China, 25–27 October 2003; pp. 76–83.
46. Hartmut, H.; Aumann, H.; Miller, C.R. Atmospheric infrared sounder (AIRS) on the earth observing system. In *Advanced and Next-Generation Satellites*; SPIE: Bellingham, WA, USA, 1995; Volume 2583, pp. 332–343.
47. Chahine, M.T.; Pagano, T.; Aumann, H.; Atlas, R.; Barnet, C.; Blaisdell, J.; Chen, L.; Divakarla, M.; Fetzer, E.; Goldberg, M.; et al. AIRS: Improving weather forecasting and providing new data on greenhouse gases. *Bull. Am. Meteorol. Soc.* **2006**, *87*, 911–926. [CrossRef]
48. Menzel, W.P.; Schmit, T.J.; Zhang, P.; Li, J. Satellite-Based Atmospheric Infrared Sounder Development and Applications. *Bull. Am. Meteorol. Soc.* **2018**, *99*, 583–603. [CrossRef]
49. Kummerow, C.; Simpson, J.; Thiele, O.; Barnes, W.; Chang, A.T.C.; Stocker, E.; Adler, R.F.; Hou, A.; Kakar, R.; Wentz, F.; et al. The Status of the Tropical Rainfall Measuring Mission (TRMM) after Two Years in Orbit. *J. Appl. Meteorol.* **2000**, *39*, 1965–1982. [CrossRef]
50. Liu, Z.; Ostrenga, D.; Teng, W.; Kempler, S. Tropical Rainfall Measuring Mission (TRMM) Precipitation Data and Services for Research and Applications. *Bull. Am. Meteorol. Soc.* **2012**, *93*, 1317–1325. [CrossRef]
51. Sneyers, R. *On the Statistical Analysis of Series of Observations; Technical Note No. 143*; World Meteorological Organization (WMO): Geneva, Switzerland, 1990.
52. Mosmann, V.; Castro, A.; Fraile, R.; Dessens, J.; Sanchez, J. Detection of statistically significant trends in the summer precipi-tation of mainland Spain. *Atmos. Res.* **2004**, *70*, 43–53. [CrossRef]
53. Cleveland, R.B.; Cleveland, W.S.; McRae, J.E.; Terpenning, I.J. STL: A seasonal-trend decomposition procedure based on loess. *J. Off. Stat.* **1990**, *6*, 3–33.
54. Rosner, B. Percentage points for a generalized ESD many-outlier procedure. *Technometrics* **1983**, *25*, 165172. [CrossRef]
55. Ryu, M.; Lee, G.; Lee, K. Online sequential extreme studentized deviate tests for anomaly detection in streaming data with varying patterns. *Clust. Comput.* **2021**, *24*, 1975–1987. [CrossRef]
56. Barbosa, P.M.; Stroppiana, D.; Grégoire, J.-M. An assessment of vegetation fire in Africa (1981–1991): Burned areas, burned biomass, and atmospheric emissions. *Global Biogeochem. Cy.* **1999**, *13*, 933–950. [CrossRef]
57. Liu, Z.; Murphy, J.; Maghirang, R.; Devlin, D. Health and Environmental Impacts of Smoke from Vegetation Fires: A Review. *J. Environ. Prot. Sci.* **2016**, *7*, 1860–1885. [CrossRef]
58. Haywood, J.; Osborne, S.R.; Francis, P.N.; Keil, A.; Formenti, P.; Andreae, M.O.; Kaye, P.H. The mean physical and optical properties of regional haze dominated by biomas burning aerosol measured from the C-130 aircraft during SAFARI 2000. *J. Geophys. Res* **2003**, *108*, 8473.
59. Winkler, K.; Gessner, U.; Hochschild, V. Identifying droughts affecting agriculture in Africa based on remote sensing time series between 2000–2016: Rainfall anomalies and vegetation condition in the context of ENSO. *Remote Sens.* **2017**, *9*, 831. [CrossRef]
60. D'abreton, P.C.; Lindesay, J. A, Water vapour transport over Southern Africa duringwet and dry early and late summer months. *Int. J. Climatol.* **1993**, *13*, 151–170. [CrossRef]

61. Masinda, M.M.; Sun, L.; Wang, G.; Hu, T. Moisture content thresholds for ignition and rate of fire spread for various dead fuels in northeast forest ecosystems of China. *J. For. Res* **2021**, *32*, 1147–1155. [CrossRef]
62. Possell, M.; Bell, T.L. The influence of fuel moisture content on the combustion of Eucalyptus foliage. *Int. J. Wildland Fire* **2013**, *22*, 343–352. [CrossRef]
63. Diffenbaugh, N.S.; Koning, A.G.; Field, C.B. Atmospheric variability contributes to increasing wildfire weather but not as much as global warming. *Proc. Natl. Acad. Sci. USA* **2021**, *118*, e2117876118. [CrossRef]
64. Holden, Z.A.; Swanson, A.; Luce, C.H.; Jolly, W.M.; Maneta, M.; Oyler, J.W.; Warren, D.A.; Parsons, R.; Affleck, D. Decreasing fire season precipitation increased recent western US forest wildfire activity. *Proc. Natl. Acad. Sci. USA* **2018**, *115*, E8349–E8357. [CrossRef] [PubMed]
65. Qu, C.; Hao, X.; Qu, J.J. Monitoring extreme agricultural drought over the horn ofafrica (hoa) using remote sensing measurements. *Remote Sens.* **2019**, *11*, 902. [CrossRef]
66. Brenner, J. Southern Oscillation Anomalies and Their Relationship to Wildfire Activity in Florida. *Int. J. Wildland Fire* **1991**, *1*, 73–78. [CrossRef]